MATERIALS SCIENCE

Three-dimensional printing of functionally graded liquid crystal elastomer

Zijun Wang[1], Zhijian Wang[2]*, Yue Zheng[2], Qiguang He[2], Yang Wang[1], Shengqiang Cai[1,2]*

Copyright © 2020 The Authors, some rights reserved; exclusive licensee American Association for the Advancement of Science. No claim to original U.S. Government Works. Distributed under a Creative Commons Attribution NonCommercial License 4.0 (CC BY-NC).

As a promising actuating material, liquid crystal elastomer (LCE) has been intensively explored in building diverse active structures and devices. Recently, direct ink writing technique has been developed to print LCE structures with various geometries and actuation behaviors. Despite the advancement in printing LCE, it remains challenging to print three-dimensional (3D) LCE structures with graded properties. Here, we report a facile method to tailor both the actuation behavior and mechanical properties of printed LCE filaments by varying printing parameters. On the basis of the comprehensive processing-structure-property relationship, we propose a simple strategy to print functionally graded LCEs, which greatly increases the design space for creating active morphing structures. We further demonstrate mitigation of stress concentration near the interface between an actuatable LCE tube and a rigid glass plate through gradient printing. The strategy developed here will facilitate potential applications of LCEs in different fields.

INTRODUCTION

Liquid crystal elastomers (LCEs), which are capable of generating large reversible actuation and producing large work density, have demonstrated great potential in building novel soft robots (*1*), wearable devices (*2*), artificial muscles (*3*), and biomimetic systems (*4*, *5*). Actuation of LCEs originates from the orientation change of liquid crystal mesogens during its nematic-to-isotropic phase transition. As a result, the actuation performance of an LCE is mainly determined by the alignment of its mesogens.

Several strategies such as mechanical stretching (*6*), surface alignment (*7*), and application of magnetic/electric field (*7*–*9*) have been used to align or pattern liquid crystal mesogens in LCEs. However, each strategy has its own intrinsic limitation. For example, it is difficult to pattern mesogen orientation through mechanical stretching; surface alignment method is limited to fabricating thin-film samples (<50 μm); extremely high magnetic/electric field is required for orienting liquid crystal mesogens in an elastomer. These limitations have been restricting broader applications of LCEs in diverse fields.

Recently, direct ink writing (DIW) technique has been explored to pattern mesogen alignment in LCE structures with complex geometries. In DIW process of LCE, viscous ink composed of uncrosslinked liquid crystal oligomers is extruded out of a printing nozzle and the mesogens are spontaneously aligned along the printing path by the shear stress generated during extrusion (*10*–*15*). Structures with versatile actuation behaviors have been created through programming the local alignment of liquid crystal mesogens. The advancement in three-dimensional (3D) printing of LCE has opened a new avenue for designing and creating novel LCE-based soft robots and devices (*1*, *16*).

In the previous studies of 3D printing LCEs, filaments may follow various paths in one structure, but they often have identical properties, which are mainly determined by printing parameters such as printing temperature and nozzle size (*10*, *12*, *14*, *17*). In contrast, functionally graded materials are ubiquitous both in biology and in engineering applications (*18*). For example, mechanical properties and microstructure of the tissue in tendon-to-bone insertion (enthesis) change gradually for enhancing structural durability (*19*). Structures with graded mechanical properties have been fabricated to minimize stress concentration and to realize combined high compliance and high resilience (*20*). Bartlett *et al.* (*21*) constructed a functionally graded soft robot powered by combustion and used modulus gradient to reduce local deformation in the robot legs. Graded hip prostheses have been developed to enhance the bonding strength between implants and bones (*22*). However, soft responsive structures with both functionally graded mechanical properties and actuation performance have been seldom reported because of limited option of materials and underlying fabrication challenges.

Here, we report a facile DIW printing strategy to print functionally graded LCEs in one single structure. By controlling printing parameters, such as printing temperature, nozzle size, and distance between the nozzle and build plate, we can print LCE filaments with tailorable properties including actuation strain, actuation stress, and mechanical stiffness. We further demonstrate that with the new printing strategy, structures composed of functionally graded LCE can be fabricated, enabling more possibilities of designing active morphing structures and mitigating stress concentration near interface between distinct materials. The method developed here may further promote design and fabrication of LCE structures with versatile functionalities.

RESULTS

Strategy of printing LCE filaments with tailorable properties

Figure 1A schematically depicts the mechanism of printing LCE filaments with tailorable thermomechanical properties. The printing ink is prepared through the Michael addition reaction between liquid crystal mesogen RM257 and chain extender 2,2′-(ethylenedioxy) diethanethiol (EDDET) with acrylate moieties as the end groups (fig. S1). The degree of polymerization (fig. S2) is controlled by the feed ratio between RM257 and EDDET. During a printing process, the ink containing uncrosslinked liquid crystal oligomers (Fig. 1B showing its chemical structure) and a photo initiator (Irgacure 2959) is first heated up close to or above the nematic-isotropic phase transition

[1]Materials Science and Engineering Program, University of California, San Diego, La Jolla, CA 92093, USA. [2]Department of Mechanical and Aerospace Engineering, University of California, San Diego, La Jolla, CA 92093, USA.
*Corresponding author. Email: zhw097@eng.ucsd.edu (Z.W.); shqcai@ucsd.edu (S.C.)

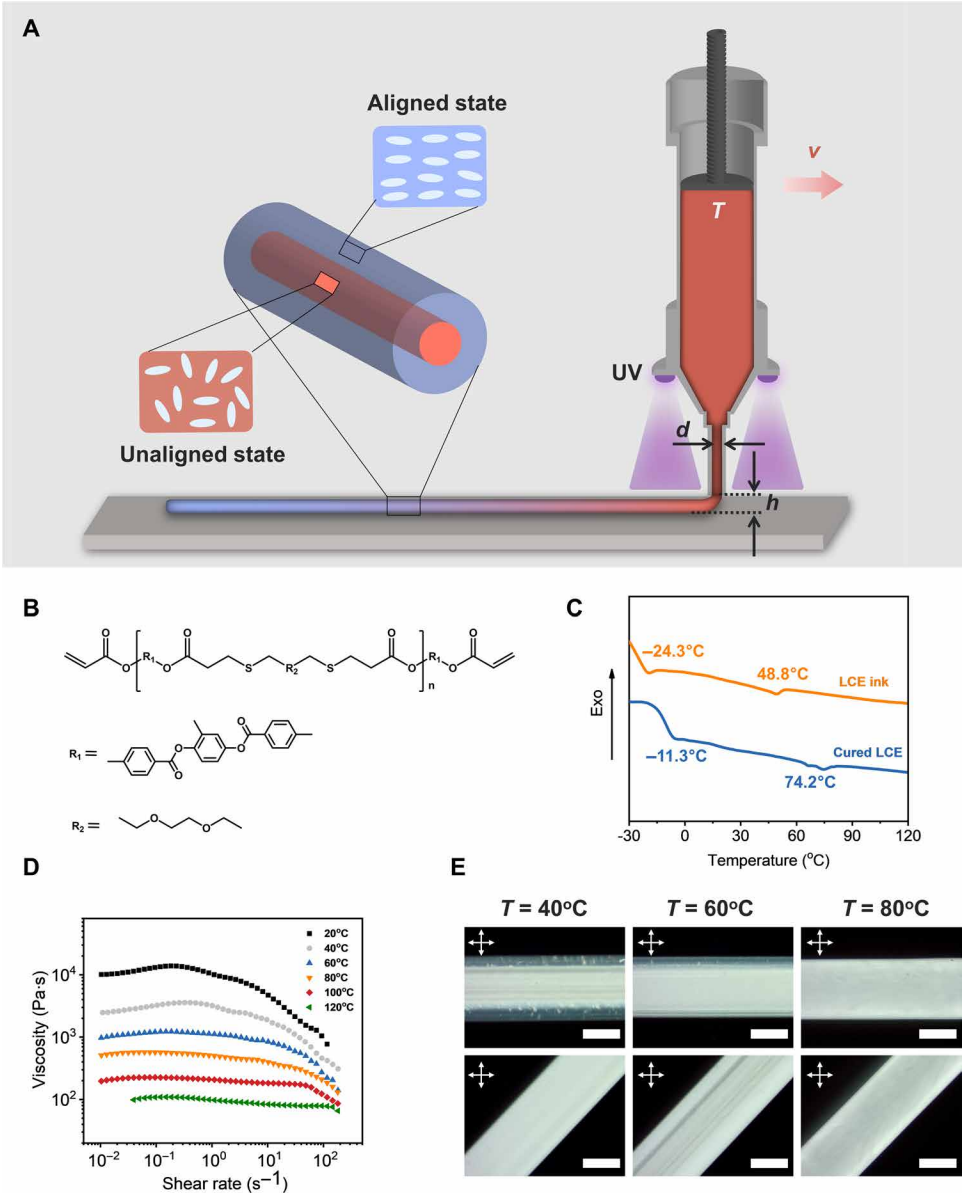

Fig. 1. DIW printing of LCE with tailorable thermomechanical properties. (**A**) Schematic illustration of the setup of DIW printing of LCE. The LCE ink is heated up to the temperature *T* and extruded out of the nozzle with an inner diameter *d*. The nozzle tip moves at a speed of *V* during the printing, and the distance between the nozzle tip and build plate is *h*. Because of the shear stress generated through the extrusion process, liquid crystal mesogens are initially aligned along the printing path. After certain period of time, the extruded LCE filament gradually cools down to room temperature and a core-shell structure forms in the filament. The outer shell of the filament cools down much faster than the inner core. As a result, well-aligned liquid crystal mesogens in the outer shell are temporarily fixed by high viscosity of the material, while the mesogens have enough time to reorientate to a polydomain state in the inner core. (**B**) Molecular structure of uncrosslinked liquid crystal oligomer in the printing ink. (**C**) DSC traces of LCE ink and cured LCE. (**D**) Viscosity of the ink as a function of shear rate at different temperatures. (**E**) Polarized optical microscope (POM) images of LCE filaments printed at different temperatures. Scale bars, 0.5 mm. Photo credit: Zijun Wang, UCSD.

temperature (T_{NI}) of the liquid crystal oligomers and then extruded out through the nozzle of a DIW 3D printer (Engine SR, Hyrel 3D).

The extruded LCE filaments are further crosslinked under ultraviolet (UV) illumination to permanently fix the mesogen alignment. After crosslinking, the glass transition temperature (T_g) and T_{NI} of the material increase from −24.3° and 48.8°C to −11.3° and 74.2°C, respectively, as determined by differential scanning calorimetry (DSC) (Fig. 1C).

During the printing process, we measure the temperature field near the printing nozzle using an infrared (IR) camera [E75-42, forward-looking infrared (FLIR)], as shown in fig. S3. There is a clear temperature drop from the syringe to the printing nozzle. For instance, when the printing temperature is set to be 40°C, the temperature of the syringe reaches 42.4°C, while the temperature of the ink exiting the nozzle is only 30.5°C, which is below T_{NI}. Similarly, for printing temperatures of 60° and 80°C, the surface temperature of the ink

exiting the nozzle reaches 39.6° and 55.8°C, respectively, which is close to or above T_{NI}. It is worth noting that the IR camera measures the surface temperature of the filament, and the temperature in the core of the filament can be slightly higher.

As reported in previous studies, liquid crystal mesogens align under shear and extensional flow along the printing path (*10–14*). Subsequently, the hot viscous filament cools down gradually to room temperature, accompanied with a marked increase of its viscosity (Fig. 1D). Before crosslinking, liquid crystal mesogens in the filament can rotate and tend to form a macroscopically unaligned state. Reorientation of mesogen takes certain period of time, which is temperature dependent. For material near the surface of the filament (shell), its temperature drops shortly. Consequently, aligned mesogens near the surface can be temporarily fixed by high viscosity of the material before their reorientation. However, for material near the center of the filament (core), which cools relatively slower, the mesogens have enough time to reorientate before the marked increase of viscosity. As a result, a core-shell structure, in which the core and the shell have different magnitudes of alignment, forms in the filament (Fig. 1A): the liquid crystal mesogens are nearly uniformly aligned in the outer shell, while the mesogen orientation in the core is random in a macroscopic scale, namely, in a polydomain state (*23*).

The assumption described above is further validated with experiments. Using polarized optical microscopy (POM), we can examine the mesogen alignment in printed LCE filaments. An extruded, single LCE filament is observed between crossed polarizers, as shown in Fig. 1E. For a filament printed at 40°C, the outer shell of the filament is dark, and the inner core is bright under POM when the axial direction of the filament is parallel to the polarizer or the analyzer. The brightness of the outer shell increases greatly when the axial direction of the filament is 45° with respect to the polarizer, indicating that the liquid crystal mesogens in the shell align along the printing path. However, the brightness of the inner core does not vary much when we rotate the filament, confirming that the inner core of the filament is in a polydomain state (*24*). With the increase of printing temperature, the volume of the shell shrinks and the shell even disappears in the filament printed at 80°C, indicating the entire filament being in a polydomain state.

A free-standing LCE filament generates thermal contraction only when the liquid crystal mesogens are aligned in a macroscopic scale. Therefore, for one filament, the aligned shell is the only contributor to its actuation behavior. The ratio between the size of core and shell determines the overall thermomechanical behavior of the filament, which can be tuned by varying printing temperature T, the distance between the nozzle and build plate h, and the inner diameter of the nozzle d, as shown in Fig. 1A. Other printing parameters, such as printing speed V and flow rate, are fixed in our experiments (see Materials and Methods for more details). We will discuss the effects of these parameters later since they may also affect the properties of LCE filaments (*25*, *26*).

Dependence of LCE filament properties on printing parameters

We next systematically study the relationship between filament properties and the following printing parameters: T (printing temperature), h (gap size, the distance between the nozzle and build plate), and d (the inner diameter of the nozzle), as shown in Fig. 2. It is found that for a fixed T and h, with an increase of d, the transparency of LCE sheets greatly reduces (Fig. 2A) under ambient light, indicating the transition from an aligned state to a polydomain state (*24*). Similarly, increasing gap size h also results in transparency decrease of printed LCE sheets, with d and T being fixed. Compared to the nozzle size and gap size, it is more convenient to tune the printing temperature during a continuous printing process. As shown in Fig. 2A, with fixed nozzle inner diameter and gap size, the printed LCE sheets are more transparent with lower printing temperature, indicating better alignment of mesogens in the elastomer.

One of the most critical parameters for describing actuation properties of an LCE is the magnitude of its actuation strain. We measure the actuation strain of single-layer free-standing LCE sheets composed of identical LCE filaments by conducting heating and cooling tests. As shown in fig. S4, the actuation strain ε_a along the direction of printing path is defined as $\varepsilon_a = -(l - l_o)/l_o$, where l_o is the original length of the LCE sheet, and l is its length at 90°C. A diagram of actuation strain of LCE sheets printed with varied printing parameters is shown in Fig. 2B. The darker color in the diagram represents larger actuation strain. We find that the magnitude of actuation strain of printed LCE sheets is consistent with their appearance: Generally speaking, sheets with higher transparency have larger actuation strain. With higher printing temperature, larger gap size, or larger nozzle inner diameter, the actuation strain decreases. As changing nozzle during continuous printing can be inconvenient in general, d is fixed at 0.838 mm (18 gauge) for later discussion if not specially noted.

We also measure the actuation stress of printed LCE sheets using Dynamic Mechanical Analysis apparatus (RSA-G2, TA Instruments), and the results are shown in Fig. 2C. We fix the length of the sheet while raising the temperature at a rate of 5°C/min. The actuation stress generated by the LCE sheet is measured as a function of temperature. As expected, the LCE sheet printed at higher T or larger h shows a smaller actuation stress. For example, the LCE sheet printed with h = 0.2 mm and T = 40°C shows the largest actuation stress of around 300 kPa among all samples, while the sample printed with h = 0.8 mm and T = 120°C generates almost negligible actuation stress.

On the basis of the core-shell model proposed previously, we can provide a qualitative explanation for the processing-structure-property relationship of printed LCE sheets shown in Fig. 2 (A and B) as follows: With larger gap size (h) or larger nozzle inner diameter (d), the filament has a larger radius, leading to a larger inner core in a polydomain state. At high printing temperature, the viscosity of the material is low, and thus, the time needed for the mesogens to form a polydomain state is short. As a result, aligned mesogens can only be fixed within a thin outer shell near the surface of the filament for high printing temperature. Therefore, the LCE sheets look less transparent and generate smaller actuation strain/stress when they are printed with larger gap size (h), larger nozzle inner diameter (d), or higher printing temperature (T).

In addition to the actuation strain and stress, we can also tailor the mechanical stiffness of printed LCE filaments by varying the ratio of sizes of its inner core and outer shell. We print four LCE sheets with two printing temperatures of 40° and 120°C and two gap sizes of 0.2 and 0.8 mm. Each individual sheet is composed of identical filaments. Using a mechanical testing machine (5965 Dual Column Testing System, Instron), we measure the stress-strain curve of LCE sheets with the tension force applied along the length direction. As shown in Fig. 2D, the mechanical stiffness of the LCE sheet printed at a higher temperature with a larger gap size is notably lower

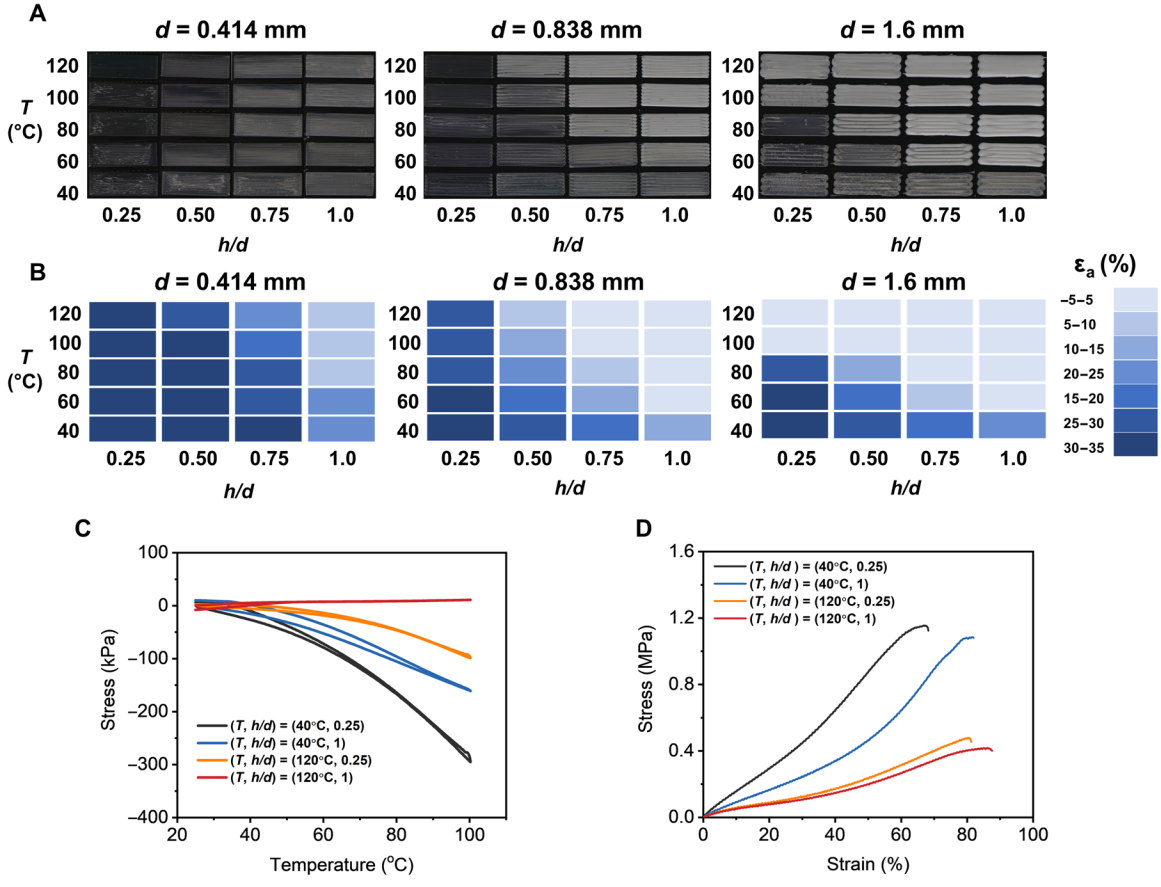

Fig. 2. Processing-property relationship of printed LCE sheets. (**A**) Optical images and (**B**) maximal actuation strain (ε_a) of printed LCE sheets obtained with different printing parameters. The printed sheet has a rectangular shape with a size of 30 mm by 10 mm by *h* (distance between the nozzle and build plate). (**C**) Actuation stress of a printed sheet as a function of temperature with a fixed strain (0%). The measured sheet has a rectangular shape with sizes of 30 mm by 10 mm by 0.2 mm or 30 mm by 10 mm by 0.8 mm. (**D**) Uniaxial tensile test results of the LCE sheets printed with different parameters. The measured sheet has a rectangular shape with sizes of 30 mm by 10 mm by 0.2 mm or 30 mm by 10 mm by 0.8 mm. The strain rate is set to be 0.1 min^{-1} during the mechanical measurements. Photo credit: Zijun Wang, UCSD.

than the one printed at a lower temperature with a smaller gap size. Inside the inner core, a polydomain structure is formed, often exhibiting soft elasticity (*27*). Consequently, with the increase of the portion of the inner core, the overall mechanical stiffness of an LCE filament decreases.

3D printing of active morphing structures with functionally graded LCE

On the basis of the relationship between LCE filament properties and printing parameters obtained above, we can construct structures with functionally graded LCE using DIW technique. As a simple demonstration, we first print several circular discs with LCE filaments oriented circumferentially, as shown in Fig. 3. The LCE discs are printed with a nozzle inner diameter *d* of 0.838 mm and a gap size *h* of 0.6 mm. The first circular LCE disc is composed of LCE filaments all printed at 40°C (Fig. 3A). When the disc is heated up in hot water of 90°C, the flat disc deforms to a conical shape, which is similar to the previous reports (*10*–*12*).

We next print three additional discs that have the same shape and same printing path as the one in Fig. 3A but with graded actuation strain. The graded LCE discs are constructed by printing their parts at several temperatures: 40°, 80°, and 120°C. On the basis of the diagram in Fig. 2B, we sketch the distribution of actuation strain in the discs, as shown in Fig. 3 (on the leftmost column). For example, in Fig. 3B, the actuation strain gradually increases from the center of the disc to its peripheral area, while the actuation strain gradually decreases from the center to the peripheral area in Fig. 3C. In Fig. 3D, the actuation strain changes from the center to its peripheral area in a nonmonotonic way. When the three discs are immersed in hot water of 90°C, they deform in markedly different manners. We further conduct finite-element analysis (FEA) to predict the active shape morphing of functionally graded LCE discs (the rightmost column of Fig. 3). Details of FEA can be found in Materials and Methods. To compare the simulated results with experiments, we measure the profile of the deformed discs using a digital camera. The quantitative comparisons between experiments and FEA simulations are shown in fig. S5. The excellent agreement between the simulation and experimental results enables us to design various active morphing structures with functionally graded LCE before fabrication.

Bilayer design has been commonly used to build morphing devices (*28*, *29*). We next show that we can combine gradient printing with bilayer design to obtain more versatile active morphing behaviors. We design bilayer structures with six petals mimicking blooming flowers and print them with the LCE ink containing fluorescent

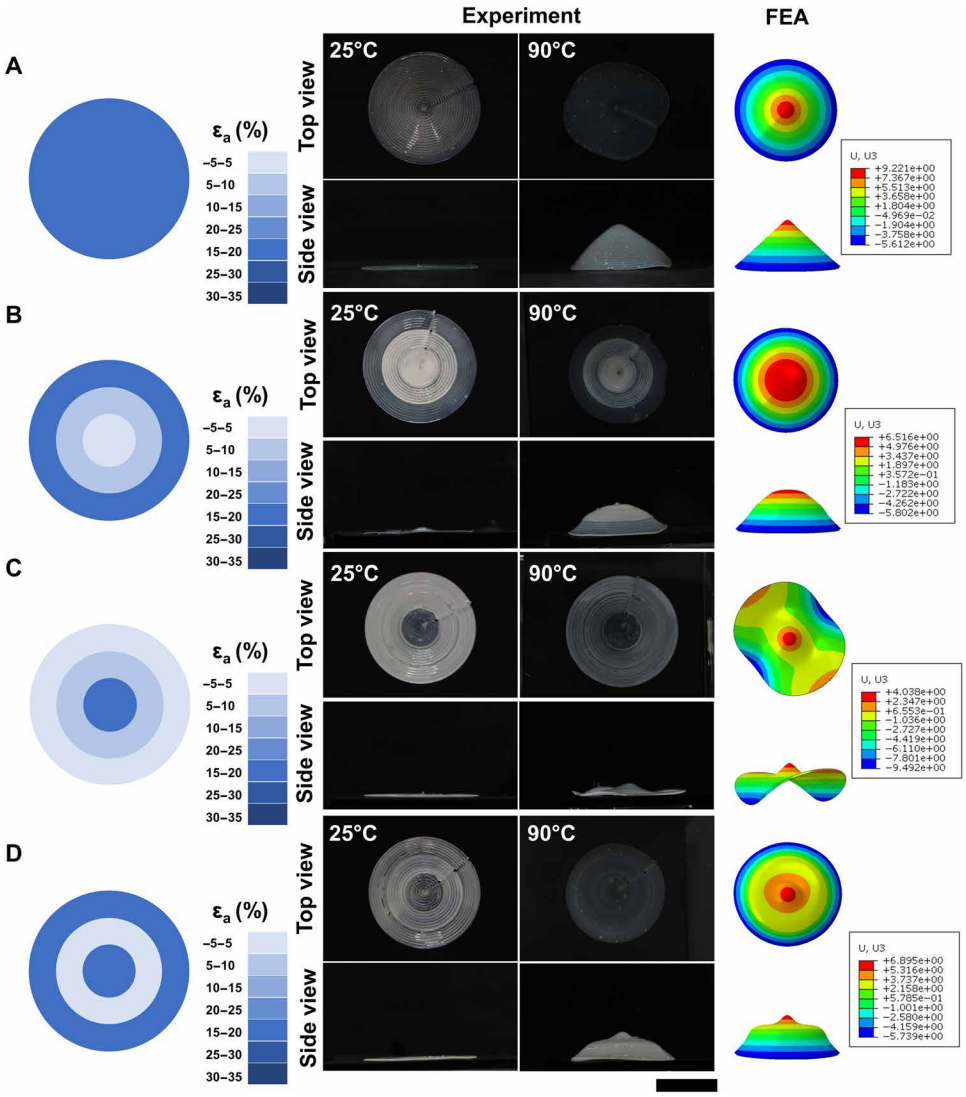

Fig. 3. 3D-printed active morphing discs with functionally graded LCE. (**A**) to (**D**) are four circular discs with LCE filaments printed circumferentially. Actuation strain of LCE filaments is homogeneous in (A) and with customized gradient in (B) to (D). The magnitude of actuation strain in each disc is represented by the darkness of the blue color in the sketch. When the discs are immersed in hot water of 90°C, the thermally induced deformation of the four discs is dramatically different from each other. FEA simulations are conducted to simulate the deformed shape. Vertical displacement field is represented by different colors. Scale bar, 20 mm. Photo credit: Zijun Wang, UCSD.

dye rhodamine B (RhB). For the center part of the structure, as shown in Fig. 4, a simple concentric printing path is adopted. In Fig. 4A, each layer of the petals is printed with the same parameters ($h = 0.6$ mm and $T = 40$°C), but the angle between the printing path in the bottom and top layer is set to be 90°. After immersed in hot water of 90°C, each petal twists with its chirality fully determined by the printing path. In Fig. 4B, each petal is composed of one bottom layer with negligible actuation strain and one top layer with maximal actuation along the length direction. When immersed in hot water of 90°C, each petal curls up homogeneously due to the contraction mismatch between the two layers. In Fig. 4 (C and D), by controlling the printing temperature, we print each petal with graded actuation strain in the top layer, in addition to the contraction mismatch between top and bottom layers. Although each petal still bends up when they are heated in hot water, their bending morphologies are quite distinct because of the various planar gradient of actuation strain in the top layer. Likewise, we conduct FEA simulation to predict the deformation of the bilayer structures, as shown in Fig. 4. The quantitative comparisons between experiments and FEA predictions of the deformation of the petals are shown in fig. S6.

Active auxetic lattice structures composed of graded LCE

Lattice structures with negative Poisson's ratio, also known as auxetic structures, have shown great potential in various applications, such as energy adsorption, deployable devices, and robotic systems (*30–33*). The Poisson's ratio of a lattice structure is usually only determined by its geometry and is fixed after the completion of fabrication (*30*). However, lattice structures, for a fixed geometry, being able to exhibit different Poisson's ratios may be desired in real applications (*33*). For example, hybrid lattice structures with distributed negative and

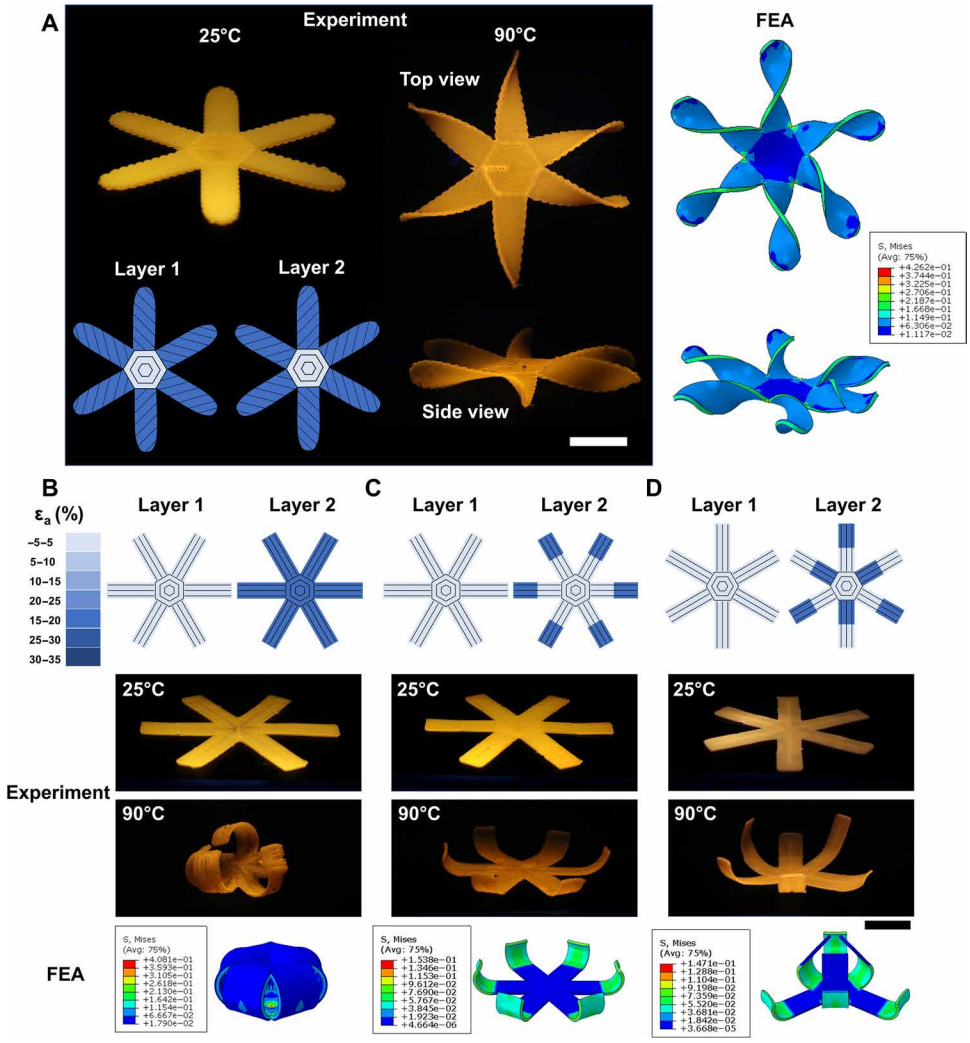

Fig. 4. 3D-printed LCE bilayer structures with six petals. Fluorescent dye RhB is added to the ink for printing these structures. All photos are taken under 365-nm UV illumination. (**A**) Each petal is composed of two layers of LCE with different printing paths but the same printing parameters. The angle between the two printing paths in two layers is 90°. When the bilayer structure is immersed in hot water of 90°C, all petals twist. (**B** to **D**) The printing paths of two layers of petals are the same (along the length direction). In addition, for the bottom layer, the LCE is printed with minimal actuation strain. For the top layer of a petal, the actuation strain is homogeneous in (B) but with customized gradient in (C) and (D). When the bilayer structures are immersed in hot water of 90°C, their bending morphologies are distinct from each other in (B) to (D). FEA simulations are conducted to calculate the deformed shapes of the printed bilayer structures. The stress field is represented by different colors. The gradient printing strategy increases the design space for active morphing structures. Scale bars, 20 mm. Photo credit: Zijun Wang, UCSD.

positive Poisson's ratio have shown advantages as biological implants over traditional materials (*34*). In the demonstrated example of a hybrid structure (*34*), the variation of the Poisson's ratio is achieved by the change of lattice geometry. As a result, the compatibility between lattices with different geometries must be carefully considered during the design. Therefore, if a lattice with a fixed geometry can exhibit different Poisson's ratios, constructing a structure with distributed Poisson's ratio can be greatly simplified. In some other applications, it can be very useful that the Poisson's ratio of a lattice structure is tunable by external stimuli (*31*–*33*).

In the current work, as a proof-of-concept demonstration, we print two auxetic lattice structures with the same re-entrant honeycomb shape but with different combinations of LCE filaments, as shown in Fig. 5. We then apply uniaxial stretch onto two lattice structures at both room temperature and 100°C. The Poisson's ratio of the structure is determined by measuring the size change of a rectangular unit selected from the lattice, as shown in Fig. 5 (A and B). The Poisson's ratio is calculated by the following equation: $\upsilon = -\varepsilon_y/\varepsilon_x$, where ε_x is the true strain in the loading direction and ε_y is the true strain in the transverse direction.

For the first lattice structure (Fig. 5A), the serrated beams have a maximum actuation strain of around 20% (indicated in deep blue) and the vertical beams do not contract (indicated in light blue). As shown in Fig. 5C, at room temperature, the Poisson's ratio of the structure starts from −2.1 with small stretch and approaches −0.5 as it is highly stretched. At 100°C, the serrated beams contract and the cell angle θ (as defined in Fig. 5A) becomes larger in the lattice. With the increase of the stretch, the Poisson's ratio of the structure starts from 0.6 and gradually decreases to 0.25 when the applied true strain equals 0.28. For the second lattice structure (Fig. 5B), the serrated

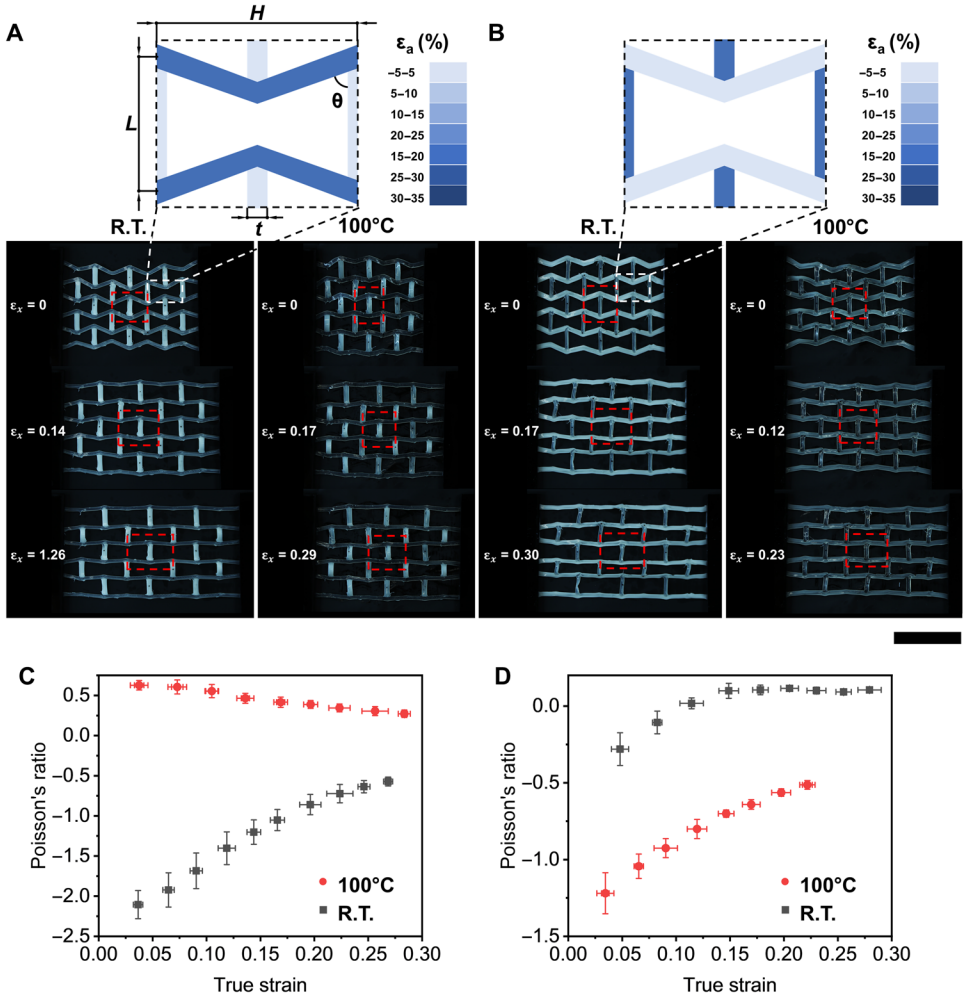

Fig. 5. Active auxetic lattice structures composed of functionally graded LCE. In the design (**A**), the serrated beams have a maximum actuation strain of around 20% (indicated in deep blue), and the vertical beams do not contract (indicated in light blue). (**B**) The serrated beams have negligible actuation strain, and the vertical beams have a maximum actuation strain of around 20%. (**C**) Relation between calculated Poisson's ratio and true strain for the structure in (A). At room temperature (R.T.), the Poisson's ratio of the structure is negative, which increases with the applied stretch. At high temperature, the Poisson's ratio of the structure is positive and insensitive to the applied stretch. (**D**) Relation between measured Poisson's ratio and true strain for the structure in (B). At room temperature, the Poisson's ratio of the structure is negative with small stretch and gradually increases to a small positive value with the increase of the stretch. A notable decrease of the Poisson's ratio occurs when the temperature is increased to 100°C. The rectangular unit (in red) is marked to calculate true strain in loading direction (ε_x) and in transverse direction (ε_y). $L = 11.55$ mm, $H = 16.8$ mm, $t = 1.7$ mm, initial $\theta = 69.44°$. Scale bar, 30 mm. Photo credit: Zijun Wang, UCSD.

beams have a negligible actuation strain and the vertical beams have a maximum actuation strain of around 20%. At room temperature, the Poisson's ratio of the structure starts from −0.25 and increases to 0.1 as the true strain reaches 0.25 (Fig. 5D). At 100°C, the vertical beams contract, making the whole structure narrower in transverse direction but the cell angle θ remains almost the same. Consequently, at high temperature, the Poisson's ratio of the second lattice structure changes with the applied stretch following a similar trend as that at room temperature, while the values of the Poisson's ratio are changed notably because of the temperature variation. The experimental results shown in Fig. 5 have demonstrated that the Poisson's ratio of a graded LCE lattice structure can be tuned by changing environmental temperature. By comparing the results in Fig. 5 (C and D), we have further shown that the Poisson's ratio of a graded LCE lattice structure can be varied while maintaining lattice design unchanged. The strategy demonstrated here may facilitate more practical applications of auxetic lattice structures.

Mitigation of stress concentration near LCE-passive material interface

The interfaces between a soft material and a hard material (e.g., tendon and bone) or an active material and passive material (e.g., actuator and controlling system) can be commonly found in complex structures in both biology and engineering applications (*19*, *21*, *35*). Severe stress concentration often happens near the interface of two materials with contrast properties, which may lead to failure of the structure. One strategy to mitigate such stress concentration is by using functionally graded material as a transition (*36*–*38*).

Here, as a proof-of-concept demonstration, we print a hollow soft LCE tube on the top of a nonresponsive rigid glass plate. The LCE

can adhere to the glass surface through van der Waals interaction. Similar structures have been explored to construct tubular grippers (*39*) and robotic feet (*1*). In the tube, the LCE filaments are aligned circumferentially in each layer. As shown in Fig. 6A and movie S2, if the tube is composed of LCE filaments with identical properties, with the increase of temperature, the tube contracts in the radial direction and finally detaches from the glass plate when the environmental temperature reaches 94°C, due to the large stress concentration near the interface. As a comparison, we print another LCE tube with the same geometry but gradually varied actuation strain, as shown in Fig. 6B. Near the interface between the tube and the glass plate, the LCE has minimal actuation, while the LCE filaments have the largest actuation on the free end of the tube. For the LCE tube with the gradient properties, with the increase of temperature, the bottom stays attached to the rigid plate, while the free end of the tube shrinks notably in the radial direction. FEA simulations of the stress field of the LCE tubes attached on a rigid substrate are shown in Fig. 6C (details of the simulations can be found in Materials and Methods). As the simulation result indicates, the stress near the interface between graded LCE tube and the glass plate is substantially lower.

DISCUSSION

Here, we have developed a facile way to print functionally graded LCE structures with customizable properties. Through systematic optical, thermal, and mechanical characterizations, we have obtained a comprehensive processing-structure-property relationship of the printed LCE filaments. To explain the experimental results, we have proposed a core-shell model for LCE filament printed by DIW method. On the basis of the relationship between printing parameters and the properties of printed filaments, we have further fabricated versatile active morphing structures with functionally graded LCE and demonstrated a strategy of mitigating stress concentration near the interface between two materials with substantially different modulus.

In most previous researches on designing and constructing active morphing structures, either the magnitude of actuation strain or actuation orientation is controlled (*40*, *41*). For instance, the distribution of crosslinking density and thus the swelling ratio of a gel can be precisely tuned through photocrosslinking process, leading to programmable active morphing behaviors (*42*, *43*). Compared with those previous methods, the printing strategy developed here allows us to control both the direction and magnitude of actuation strain at the same time, which enables much larger design space for creating active morphing systems.

It is worth mentioning that although we have demonstrated that the properties of printed LCE filaments can be tailored by changing printing temperature, more precise or finer tunability of the material properties may require better control of the thermal environment during the printing process, such as the temperature of the build plate and the convective cooling condition. Because the viscosity of LCE ink is highly sensitive to temperature, as shown in Fig. 1D, the flow rate during the extrusion process should be further optimized at different temperatures to obtain continuous and homogeneous printing filaments.

In addition, we have not discussed the effects of printing speed on the properties of printed LCE in the current work. Nevertheless, in real applications, changing printing speed may be even more

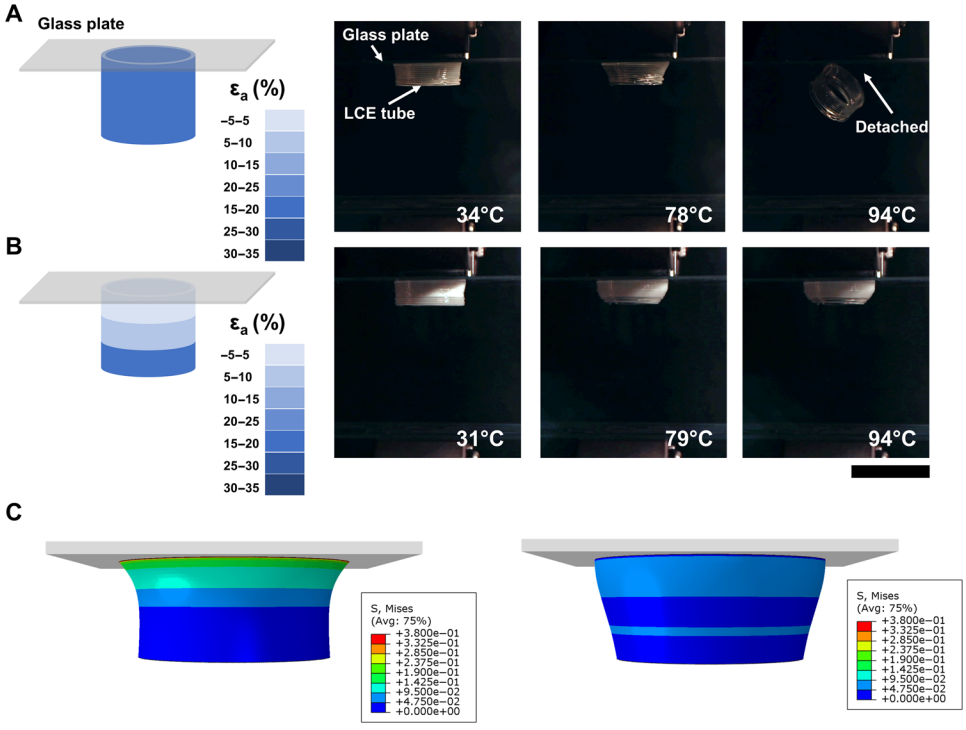

Fig. 6. Demonstration of mitigating stress concentration near the interface between an active LCE tube and a glass plate. (**A**) Homogeneous LCE tube printed on a rigid glass plate. When the tube is heated to 94°C, the tube detaches from the glass plate. (**B**) LCE tube with gradient properties printed on a rigid glass plate. The tube stays attached to the glass plate when the temperature is increased to 94°C. (**C**) FEA simulations of the stress field of the tubes at 94°C with homogeneous properties (left) and graded properties (right). The stress field is represented by different colors. Scale bar, 20 mm. Photo credit: Zijun Wang, UCSD.

convenient as compared to changing printing temperature. However, we find that with the current LCE ink, changing printing speed is not a very effective way to tune the mechanical properties and actuation performance of printed LCE filaments. We compare the actuation strain of LCE sheets obtained from three different printing speeds ranging from 0.2 to 2 mm/s and at two printing temperatures, as shown in fig. S7. It can be seen that the magnitude of actuation strain of printed LCE sheets is not very sensitive to printing speed change. However, we believe that it is still highly possible to use printing speed to effectively control the properties of printed LCE, by modifying the ink recipe and adjusting other printing parameters. Such systematic exploration is beyond the scope of the current work.

At last, we want to point out that more functionalities of printed LCE structures can be obtained with further modifications of printing ink. For instance, by introducing dynamic covalent bonds into the ink (*15*), the printed LCE structures may be recyclable, self-repairable, and reprogrammable (*44*, *45*). Photothermal agents could also be integrated into the ink, so the printed structure can be light responsive. The printing strategy developed here provides a simple platform for constructing functionally graded structures with various functionalities, which can find their applications in diverse fields.

MATERIALS AND METHODS

Materials

(1,4-Bis-[4-(3-acryloyloxypropyloxy) benzoyloxy]-2-methylbenzene) (RM257) (Wilshire Technologies, 95%), EDDET (Sigma-Aldrich, 95%), dipropylamine (Sigma-Aldrich, 98%), (2-hydroxyethoxy)-2-methylpropiophenone (Irgacure 2959, Sigma-Aldrich, 98%), RhB (Sigma-Aldrich), and methylene chloride (CH_2Cl_2) are used as received without further purification.

Preparation of LCE ink

The LCE ink is prepared by the Michael addition reaction between liquid crystal mesogens RM257 and chain extender EDDET. RM257 (8.2404 g, 14 mmol) is dissolved in 50 ml of CH_2Cl_2. Then, chain extender EDDET (2.1876 g, 12 mmol) and catalyst dipropylamine (0.100 g, 1 mmol) are added into the mixture dropwisely. The solution is stirred at room temperature overnight. After that, a photoinitiator (Irgacure 2959, 0.0500 g, 0.2 mmol) is added into the solution. It is noted that for some of the experiments (Fig. 4), the RhB dye (0.0010 g, 0.002 mmol) is added together with Irgacure 2959 into the solution. Then, the mixture is left in an oven of 85°C for 24 hours to allow complete evaporation of the solvent.

3D printing of functionally graded LCE structures

LCE ink is first loaded into a steel syringe, and the syringe is left in an oven at 85°C overnight to allow the removal of bubbles inside. Then, the syringe with LCE ink is loaded to a DIW 3D printer (Engine SR, Hyrel 3D). Structures are printed at different conditions and cured with continuous illumination of 365-nm UV light-emitting diodes (LEDs) during printing, as shown in movie S1. Printing path is controlled by customized G-code. Printing speed V is fixed at 2 mm/s. The flow rate is automatically calculated as the product of printing path width, layer height, printing speed, and a flow rate multiplier by software. After printing, structures are removed from the build plate and placed under a UVP B100-AP high-intensity UV lamp (365 nm) for 15 min for further curing. LCE tubes are first printed on glass slides and are removed from the build plate together with the slides for further curing. The surface temperature field of the syringe and nozzle during printing is measured using an IR camera (E75-42, FLIR).

Characterization of LCE ink

^{1}H nuclear magnetic resonance (NMR) spectroscopy measurement is conducted on a JEOL ECA 500 spectrometer at room temperature.

DSC measurements are carried out using Discovery DSC250 (TA Instruments) in a nitrogen atmosphere. The samples are sealed in the aluminum pans. The measurements are performed at a scanning rate of 5°C/min during heating and cooling processes in a temperature range between −35° and 150°C.

The rheological characterization of LCE ink is conducted using the Discovery HR-3 Rheometer (TA Instruments). All experiments are conducted with a 20-mm steel Peltier plate and 0.5-mm gap size. The oscillatory tests are conducted with a fixed frequency of 1 Hz.

Characterization of printed LCE

The optical images are taken using a digital camera (Canon). The POM images are taken using a ZEISS polarized microscope. Actuation strain is measured by heating and cooling printed LCE sheets between 90°C and room temperature using a hot plate. The definition of actuation strain is shown in fig. S4. The measured sample has a dimension of 30 mm by 10 mm by h (single layer). For each sample, three cycles of heating and cooling are conducted.

Dynamic mechanical analysis tests are conducted on RSA-G2 (TA Instruments), with sample dimensions of 30 mm by 10 mm by 0.2 mm and 30 mm by 10 mm by 0.8 mm. The actuation stress is measured with the LCE sheet being fixed at the original length, while the sample is heated from 25° to 100°C and then cooled down to 25°C. The heating/cooling rate is fixed at 5°C/min for all tests.

The uniaxial mechanical tests are conducted on the Universal Mechanical Testing System (5965 Dual Column Testing System, Instron) with a 5-kN loading cell. The ends of the samples are glued onto acrylic plates, which are clamped by the grippers of the mechanical testing machine. The LCE samples are tested as printed with a rectangular shape and dimensions of 30 mm by 10 mm by 0.2 mm and 30 mm by 10 mm by 0.8 mm. The engineering strain rate is set as 0.1 min^{-1} for the mechanical tests.

Demonstration of shape morphing, active auxetic structure, and stress concentration mitigation

Experiments of thermally induced actuation of printed LCE structures in Figs. 3 and 4 are conducted in a water tank with hot water (~90°C). For Fig. 4, the samples are further illuminated by 365-nm UV light to produce the fluorescent effect. To obtain the profile of the deformed LCE structures, we take photos from the front view and use ImageJ to measure the geometrical information. For each sample, three independent measurements are conducted.

To measure the Poisson's ratios of printed auxetic lattice structures, we first mark four points on a printed lattice. The four points can be regarded as four corners of a rectangular unit, as shown in Fig. 5. We then manually stretch the samples using customized stretcher at room temperature or on a hot plate at 100°C. During the stretch, we take photos of the lattice structure at different stretch ratios. We finally process the photos using ImageJ to obtain the sizes of the rectangular units during the deformation, based on which we can calculate the Poisson's ratio.

Experiments of thermally induced actuation of LCE tubes shown in Fig. 6 are conducted by heating printed LCE tubes in a temperature-controlled chamber (Instron). All samples are heated from 25° to 100°C at a rate of about 24°C/min.

FEA of the deformation of 3D-printed LCE structures

FEA is conducted using commercial software Abaqus. LCE is modeled as linear thermoelastic material with anisotropic thermal expansion coefficient and with Poisson's ratio being set as 0.499. The thermal expansion coefficient α (α is negative) in the direction parallel to the axial direction of the printed LCE filament is obtained from the measurements shown in Fig. 2B, and the thermal expansion coefficients in the directions perpendicular to the axial direction are given as $-\alpha/2$. In the simulations, the structures in Figs. 3 and 4 are in free-standing states, while LCE tubes in Fig. 6C are fixed on their top. Similar to the experiments, the deformation of a structure is induced by increasing the temperature homogeneously in the simulation. To break the symmetry of the structure in Fig. 3 (A to D), a slightly higher temperature is applied on the bottom surface of the disc. The vertical displacement fields in Fig. 3 (A to D) are in the unit of millimeters, and the stress fields in Figs. 4 and 6C are normalized by Young's modulus of the material.

SUPPLEMENTARY MATERIALS

Supplementary material for this article is available at http://advances.sciencemag.org/cgi/content/full/6/39/eabc0034/DC1

REFERENCES AND NOTES

1. Q. He, Z. Wang, Y. Wang, A. Minori, M. T. Tolley, S. Cai, Electrically controlled liquid crystal elastomer–based soft tubular actuator with multimodal actuation. *Sci. Adv.* **5**, eaax5746 (2019).
2. D. J. Roach, C. Yuan, X. Kuang, V. C.-F. Li, P. Blake, M. L. Romero, I. Hammel, K. Yu, H. J. Qi, Long liquid crystal elastomer fibers with large reversible actuation strains for smart textiles and artificial muscles. *ACS Appl. Mater. Interfaces* **11**, 19514–19521 (2019).
3. Q. He, Z. Wang, Z. Song, S. Cai, Bioinspired design of vascular artificial muscle. *Adv. Mater. Technol.* **4**, 1800244 (2019).
4. C. Ahn, X. Liang, S. Cai, Bioinspired design of light-powered crawling, squeezing, and jumping untethered soft robot. *Adv. Mater. Technol.* **4**, 1900185 (2019).
5. H. Shahsavan, S. M. Salili, A. Jákli, B. Zhao, Smart muscle-driven self-cleaning of biomimetic microstructures from liquid crystal elastomers. *Adv. Mater.* **27**, 6828–6833 (2015).
6. C. M. Yakacki, M. Saed, D. P. Nair, T. Gong, S. M. Reed, C. N. Bowman, Tailorable and programmable liquid-crystalline elastomers using a two-stage thiol–acrylate reaction. *RSC Adv.* **5**, 18997–19001 (2015).
7. T. H. Ware, M. E. McConney, J. J. Wie, V. P. Tondiglia, T. J. White, Voxelated liquid crystal elastomers. *Science* **347**, 982–984 (2015).
8. A. Buguin, M.-H. Li, P. Silberzan, B. Ladoux, P. Keller, Micro-actuators: When artificial muscles made of nematic liquid crystal elastomers meet soft lithography. *J. Am. Chem. Soc.* **128**, 1088–1089 (2006).
9. C. M. Spillmann, J. Naciri, B. Ratna, R. L. Selinger, J. V. Selinger, Electrically induced twist in smectic liquid–crystalline elastomers. *J. Phys. Chem. B* **120**, 6368–6372 (2016).
10. A. Kotikian, R. L. Truby, J. W. Boley, T. J. White, J. A. Lewis, 3D printing of liquid crystal elastomeric actuators with spatially programed nematic order. *Adv. Mater.* **30**, 1706164 (2018).
11. M. O. Saed, C. P. Ambulo, H. Kim, R. De, V. Raval, K. Searles, D. A. Siddiqui, J. M. O. Cue, M. C. Stefan, M. R. Shankar, T. H. Ware, Molecularly-engineered, 4D-printed liquid crystal elastomer actuators. *Adv. Funct. Mater.* **29**, 1806412 (2019).
12. C. P. Ambulo, J. J. Burroughs, J. M. Boothby, H. Kim, M. R. Shankar, T. H. Ware, Four-dimensional printing of liquid crystal elastomers. *ACS Appl. Mater. Interfaces* **9**, 37332–37339 (2017).
13. D. J. Roach, X. Kuang, C. Yuan, K. Chen, H. J. Qi, Novel ink for ambient condition printing of liquid crystal elastomers for 4D printing. *Smart Mater. Struct.* **27**, 125011 (2018).
14. M. López-Valdeolivas, D. Liu, D. J. Broer, C. Sánchez-Somolinos, 4D printed actuators with soft-robotic functions. *Macromol. Rapid Commun.* **39**, 1700710 (2018).
15. E. C. Davidson, A. Kotikian, S. Li, J. Aizenberg, J. A. Lewis, 3D printable and reconfigurable liquid crystal elastomers with light-induced shape memory via dynamic bond exchange. *Adv. Mater.* **32**, 1905682 (2020).
16. A. Kotikian, C. McMahan, E. C. Davidson, J. M. Muhammad, R. D. Weeks, C. Daraio, J. A. Lewis, Untethered soft robotic matter with passive control of shape morphing and propulsion. *Sci. Robot.* **4**, eaax7044 (2019).
17. C. Zhang, X. Lu, G. Fei, Z. Wang, H. Xia, Y. Zhao, 4D printing of a liquid crystal elastomer with a controllable orientation gradient. *ACS Appl. Mater. Interfaces* **11**, 44774–44782 (2019).
18. Y. Miyamoto, W. Kaysser, B. Rabin, A. Kawasaki, R. G. Ford, *Functionally Graded Materials: Design, Processing and Applications* (Springer Science & Business Media, 2013), vol. 5.
19. A. G. Schwartz, J. D. Pasteris, G. M. Genin, T. L. Daulton, S. Thomopoulos, Mineral distributions at the developing tendon enthesis. *PLOS ONE* **7**, e48630 (2012).
20. K. Kumar, J. Liu, C. Christianson, M. Ali, M. T. Tolley, J. Aizenberg, D. E. Ingber, J. C. Weaver, K. Bertoldi, A biologically inspired, functionally graded end effector for soft robotics applications. *Soft Robot.* **4**, 317–323 (2017).
21. N. W. Bartlett, M. T. Tolley, J. T. B. Overvelde, J. C. Weaver, B. Mosadegh, K. Bertoldi, G. M. Whitesides, R. J. Wood, A 3D-printed, functionally graded soft robot powered by combustion. *Science* **349**, 161–165 (2015).
22. H. Hedia, N. Fouda, Design optimization of cementless hip prosthesis coating through functionally graded material. *Comput. Mater. Sci.* **87**, 83–87 (2014).
23. S. Gantenbein, K. Masania, W. Woigk, J. P. W. Sesseg, T. A. Tervoort, A. R. Studart, Three-dimensional printing of hierarchical liquid-crystal-polymer structures. *Nature* **561**, 226–230 (2018).
24. Z. Wang, W. Fan, Q. He, Y. Wang, X. Liang, S. Cai, A simple and robust way towards reversible mechanochromism: Using liquid crystal elastomer as a mask. *Extreme Mech. Lett.* **11**, 42–48 (2017).
25. H. Yuk, X. Zhao, A new 3D printing strategy by harnessing deformation, instability, and fracture of viscoelastic inks. *Adv. Mater.* **30**, 1704028 (2018).
26. L. Ren, B. Li, Y. He, Z. Song, X. Zhou, Q. Liu, L. Ren, Programming shape morphing behavior of liquid crystal elastomers via parameter-encoded 4D printing. *ACS Appl. Mater. Interfaces* **12**, 15562–15572 (2020).
27. J. Biggins, M. Warner, K. Bhattacharya, Elasticity of polydomain liquid crystal elastomers. *J. Mech. Phys. Solids* **60**, 573–590 (2012).
28. M. Ji, N. Jiang, J. Chang, J. Sun, Near-infrared light-driven, highly efficient bilayer actuators based on polydopamine-modified reduced graphene oxide. *Adv. Funct. Mater.* **24**, 5412–5419 (2014).
29. Y. Hu, J. Liu, L. Chang, L. Yang, A. Xu, K. Qi, P. Lu, G. Wu, W. Chen, Y. Wu, Electrically and sunlight-driven actuator with versatile biomimetic motions based on rolled carbon nanotube bilayer composite. *Adv. Funct. Mater.* **27**, 1704388 (2017).
30. C. Huang, L. Chen, Negative Poisson's ratio in modern functional materials. *Adv. Mater.* **28**, 8079–8096 (2016).
31. C. Yuan, X. Mu, C. K. Dunn, J. Haidar, T. Wang, H. J. Qi, Thermomechanically triggered two-stage pattern switching of 2D lattices for adaptive structures. *Adv. Funct. Mater.* **28**, 1705727 (2018).
32. M. Lei, W. Hong, Z. Zhao, C. Hamel, M. Chen, H. Lu, H. J. Qi, 3D printing of auxetic metamaterials with digitally reprogrammable shape. *ACS Appl. Mater. Interfaces* **11**, 22768–22776 (2019).
33. Z. Zhao, C. Yuan, M. Lei, L. Yang, Q. Zhang, H. Chen, H. J. Qi, D. Fang, Three-dimensionally printed mechanical metamaterials with thermally tunable auxetic behavior. *Phys. Rev. Appl.* **11**, 044074 (2019).
34. H. M. A. Kolken, S. Janbaz, S. M. A. Leeflang, K. Lietaert, H. H. Weinans, A. A. Zadpoor, Rationally designed meta-implants: A combination of auxetic and conventional meta-biomaterials. *Mater. Horiz.* **5**, 28–35 (2018).
35. T. H. Lengyel, Y. Qi, P. Schiavone, R. Long, Interface crack between a compressible elastomer and a rigid substrate with finite slippage. *J. Mech. Phys. Solids* **90**, 142–159 (2016).
36. Q. Yang, C.-F. Gao, Reduction of the stress concentration around an elliptic hole by using a functionally graded layer. *Acta Mech.* **227**, 2427–2437 (2016).
37. T. J. Roberts, E. Azizi, Flexible mechanisms: The diverse roles of biological springs in vertebrate movement. *J. Exp. Biol.* **214**, 353–361 (2011).
38. A. Miserez, T. Schneberk, C. Sun, F. W. Zok, J. H. Waite, The transition from stiff to compliant materials in squid beaks. *Science* **319**, 1816–1819 (2008).
39. X. Qian, Q. Chen, Y. Yang, Y. Xu, Z. Li, Z. Wang, Y. Wu, Y. Wei, Y. Ji, Untethered recyclable tubular actuators with versatile locomotion for soft continuum robots. *Adv. Mater.* **30**, 1801103 (2018).
40. A. S. Kuenstler, Y. Chen, P. Bui, H. Kim, A. De Simone, L. Jin, R. C. Hayward, Blueprinting photothermal shape-morphing of liquid crystal elastomers. *Adv. Mater.* **32**, 2000609 (2020).
41. A. S. Gladman, E. A. Matsumoto, R. G. Nuzzo, L. Mahadevan, J. A. Lewis, Biomimetic 4D printing. *Nat. Mater.* **15**, 413–418 (2016).

42. Y. Zhou, C. M. Duque, C. D. Santangelo, R. C. Hayward, Biasing buckling direction in shape-programmable hydrogel sheets with through-thickness gradients. *Adv. Funct. Mater.* **29**, 1905273 (2019).
43. Z. Zhao, J. Wu, X. Mu, H. Chen, H. J. Qi, D. Fang, Origami by frontal photopolymerization. *Sci. Adv.* **3**, e1602326 (2017).
44. D. W. Hanzon, N. A. Traugutt, M. K. McBride, C. N. Bowman, C. M. Yakacki, K. Yu, Adaptable liquid crystal elastomers with transesterification-based bond exchange reactions. *Soft Matter* **14**, 951–960 (2018).
45. W. Zhijian, C. Shengqiang, Recent progress in dynamic covalent chemistries for liquid crystal elastomers. *J. Mater. Chem. B* **8**, 6610–6623 (2020).

Acknowledgments: We thank Q. Wang for the assistance in IR measurements. **Funding:** We acknowledge the support from ONR through grant no. N00014-17-1-2062 and the NSF through grant no. CMMI-1554212. **Author contributions:** Initial research directions were identified by Zijun Wang, Zhijian Wang, and S.C. Experimental investigations were conducted by Zijun Wang and Zhijian Wang, with the assistance of Q.H. and Y.W. FEA simulation was conducted by Y.Z. All authors contributed to the writing of the manuscript. **Competing interests:** The authors declare that they have no competing interests. **Data and materials availability:** All data needed to evaluate the conclusions in the paper are present in the paper and/or the Supplementary Materials. Additional data related to this paper may be requested from the authors.

Submitted 31 March 2020
Accepted 6 August 2020
Published 25 September 2020
10.1126/sciadv.abc0034

Citation: Z. Wang, Z. Wang, Y. Zheng, Q. He, Y. Wang, S. Cai, Three-dimensional printing of functionally graded liquid crystal elastomer. *Sci. Adv.* **6**, eabc0034 (2020).